



Realizing *p*-type NbCoSn half-Heusler compounds with enhanced thermoelectric performance via Sc substitution

Ruijuan Yan, Wenjie Xie, Benjamin Balke, Guoxing Chen & Anke Weidenkaff

To cite this article: Ruijuan Yan, Wenjie Xie, Benjamin Balke, Guoxing Chen & Anke Weidenkaff (2020) Realizing *p*-type NbCoSn half-Heusler compounds with enhanced thermoelectric performance via Sc substitution, *Science and Technology of Advanced Materials*, 21:1, 122-130, DOI: [10.1080/14686996.2020.1726715](https://doi.org/10.1080/14686996.2020.1726715)

To link to this article: <https://doi.org/10.1080/14686996.2020.1726715>



© 2020 The Author(s). Published by National Institute for Materials Science in partnership with Taylor & Francis Group.



[View supplementary material](#)



Accepted author version posted online: 07 Feb 2020.
Published online: 25 Feb 2020.



[Submit your article to this journal](#)



Article views: 340



[View related articles](#)



[View Crossmark data](#)

Realizing *p*-type NbCoSn half-Heusler compounds with enhanced thermoelectric performance via Sc substitution

Ruijuan Yan^a, Wenjie Xie^a, Benjamin Balke^b, Guoxing Chen^a and Anke Weidenkaff^{a,b}

^aDepartment of Materials Science, Technical University of Darmstadt, Darmstadt, Germany;

^bFraunhofer Research Institution for Materials Recycling and Resource Strategies IWKS, Alzenau, Germany

ABSTRACT

N-type half-Heusler NbCoSn is a promising thermoelectric material due to favourable electronic properties. It has attracted much attention for thermoelectric applications while the desired *p*-type NbCoSn counterpart shows poor thermoelectric performance. In this work, *p*-type NbCoSn has been obtained using Sc substitution at the Nb site, and their thermoelectric properties were investigated. Of all samples, Nb_{0.95}Sc_{0.05}CoSn compound shows a maximum power factor of 0.54 mW/mK² which is the highest among the previously reported values of *p*-type NbCoSn. With the suppression of thermal conductivity, *p*-type Nb_{0.95}Sc_{0.05}CoSn compound shows the highest measured figure of merit $ZT = 0.13$ at 879 K.

ARTICLE HISTORY

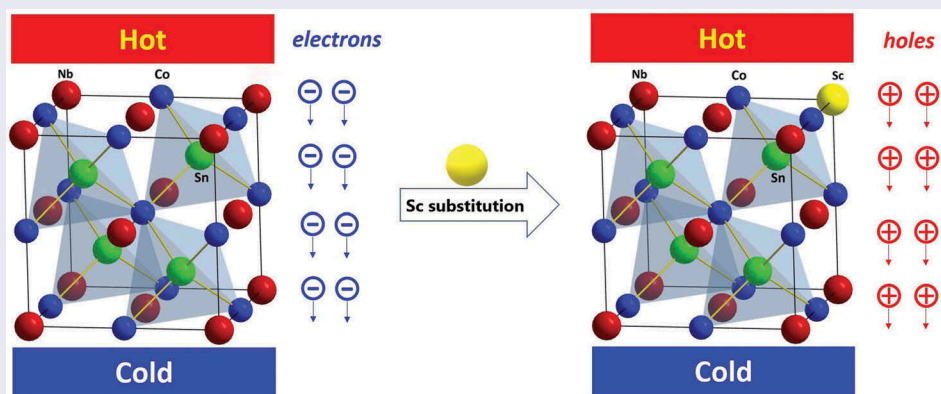
Received 23 November 2019
Revised 4 February 2020
Accepted 4 February 2020

KEYWORDS

P-type NbCoSn;
thermoelectric materials;
half-Heusler compound

CLASSIFICATION

210 Thermoelectronics;
Thermal transport;
insulators; 206 Energy
conversion; transport;
storage; recovery






1. Introduction

Thermoelectric (TE) devices can directly convert waste heat into electricity via the Seebeck effect, which is a promising reliable alternative to mechanical converters if the efficiency can be improved [1]. This could become a pathway to more sustainable energy converters in times of energy consumption [2–5]. However, up to now the application of thermoelectric devices is limited by the low energy conversion efficiency η , which is essentially decided by the materials' dimensionless figure of merit ZT : $ZT = S^2\sigma T/\kappa$ ($\kappa = \kappa_c + \kappa_l$), where S is the Seebeck coefficient, σ is the electrical conductivity, κ is the total thermal conductivity (κ_c and κ_l are the carrier and lattice components of κ , respectively), and T is the absolute temperature [6,7]. Thus, the combination of high S , σ and low κ is desirable for a large ZT . Unfortunately, these thermoelectric parameters are strongly coupled via

carrier concentration and mobility [8–10], making it difficult to optimize one single parameter without altering the others. Therefore, it has been quite challenging to develop highly efficient thermoelectric materials. The strategic goals of TE research are to discover new materials with high TE performance and/or improve the performance of the existing well-known materials, such as SiGe alloy [10], PbTe [11], chalcogenides [12], skutterudites [13,14], clathrates [15,16], Zintl phases [17] as well as full/half-Heusler compounds [18,19] by band engineering and carrier filtering effect [20–22], phonon engineering [23,24], reducing the dimension of materials [25], or spin fluctuation [26].

Due to the excellent electrical and mechanical properties, high-temperature stability, and possibility to use non-critical elements, half-Heusler (HH) compounds have become attractive candidates for thermoelectric

CONTACT Wenjie Xie  wenjie.xie@mr.tu-darmstadt.de  Department of Materials Science, Technische Universität Darmstadt, Alarich-Weiss-Straße 2, Darmstadt 64287, Germany

 Supplemental data for this article can be accessed [here](#).

© 2020 The Author(s). Published by National Institute for Materials Science in partnership with Taylor & Francis Group.

This is an Open Access article distributed under the terms of the Creative Commons Attribution License (<http://creativecommons.org/licenses/by/4.0/>), which permits unrestricted use, distribution, and reproduction in any medium, provided the original work is properly cited.

application [27–31]. This compound has a general formula XYZ (X, Y = transition metals, Z = main group elements), crystallizing in cubic $C1_b$ structure, $F\bar{4}3m$ space group [32,33]. An empirical rule proposed by Mahan and Sofo [34] states that the best thermoelectric performance is found with materials whose band gap is about $10k_B T_0$, where k_B is the Boltzmann constant and T_0 is the operating temperature of the device. NbCoSn is one of HH thermoelectric compounds with a band gap of 0.987 eV [35], and such a band gap fulfils the ' $10k_B T_0$ ' rule. In addition, the small electronegative difference between Co (1.88) and Sn (1.96) ensures larger carrier mobility. Therefore, NbCoSn is a promising mid-high temperature thermoelectric material. Unsubstituted NbCoSn is an intrinsically n -type semiconductor. In 2006 Ono et al. [36] investigated the Sb and Ti substituted n -type NbCoSn and the highest ZT of 0.3 was achieved for the $Nb_{0.99}Ti_{0.01}CoSn_{0.9}Sb_{0.1}$ at 850 K. A decade later, He et al. [37] synthesized n -type $NbCoSn_{1-x}Sb_x$ samples by arc melting combined with ball milling and hot-pressing processes, and the highest ZT reached ~ 0.6 at 1000 K for $NbCoSn_{0.9}Sb_{0.1}$. Generally, a TE device needs not only high ZT in n -type and p -type materials, but the n -type and p -type materials should have similar compositions and thus comparable mechanical properties and thermal expansion coefficient. For instance, n -type MNi (Sn,Sb) [38] and p -type MCo (Sb,Sn) [39,40] (M = Zr and Hf) compounds fulfil such criteria, and the thermoelectric module made of them reaches a record-high conversion efficiency of 12.4% with a temperature difference of 698 K [41]. To fabricate p - n NbCoSn couple, a p -type NbCoSn based compound is needed to match with the developed n -type NbCoSn compounds. However, few efforts have been devoted to investigating p -type NbCoSn. To the best of our knowledge, Ferlucchio et al. [42] first realized p -type NbCoSn via substituting Ti and Zr at Nb site, and the maximum ZT value for p -type $Nb_{0.8}Zr_{0.2}CoSn$ is only 0.03 at ~ 790 K. Obviously, the ZT value of p -type $Nb_{0.8}Zr_{0.2}CoSn$ compounds is much inferior to those of n -type counterparts. Therefore, it is crucial to identify new p -type dopants and further improve the thermoelectric performance of p -type NbCoSn.

In this work, the NbCoSn compound has been prepared through arc melting followed by annealing processes, and then Sc, chosen as a p -type dopant, is substituted at Nb site to obtain $Nb_{1-z}Sc_zCoSn$ ($z \leq 0.1$). There are two main reasons for choosing Sc as a p -type dopant: (1) The substitution of Nb (III B) by Sc (V B) can create more holes in this compound and further achieve a p -type NbCoSn. (2) The larger mass fluctuation between Nb (92.91 g/mol) and Sc (44.96 g/mol) can strengthen defect and alloying phonon scattering which can significantly suppress the lattice thermal conductivity. It is found that $Nb_{1-z}Sc_zCoSn$ compound possesses p -type conducting behaviour when $Sc = 0.05$. The highest power factor of this p -type

compound is $0.54 \text{ mW m}^{-1} \text{ K}^{-2}$, which is 230% higher than the reported value of $Nb_{0.8}Zr_{0.2}CoSn$ [42]. As a result, a peak ZT of ~ 0.13 is achieved.

2. Experimental details

$Nb_{1-z}Sc_zCoSn$ ($z \leq 0.1$) compounds were prepared by arc-melting stoichiometric amounts of the elements Nb (wire, 99.999%), Sc (piece, 99.99%), Co (bulk, 99.999%), Sn (shot, 99.999%) in Ar atmosphere. The ingots were melted several times with flipping twice over each time to ensure homogeneity. The obtained ingots were sealed into evacuated quartz tubes, annealing at 1173 K for 7 days. And then the bars and pellets for measurements were prepared by cutting these annealed ingots.

The crystal structures of samples were investigated by powder X-ray diffraction (PXRD) on a Rigaku diffractometer (Rigaku, Japan) using $Cu K_\alpha$ radiation ($\lambda_0 = 1.5418 \text{ \AA}$). The microstructures of polished samples were characterized by scanning electron microscopy (SEM; Zeiss Gemini, Germany), and the phase compositions were analyzed by energy-dispersive X-ray spectroscopy (EDX; Bruker, Germany). Electrical transport properties (Seebeck coefficient and electrical conductivity) were simultaneously measured by a ZEM-3 instrument (Ulvac-Riko, Japan) under He atmosphere from 300 to 900 K. The measurement errors for all samples are around $\pm 3\%$ (electrical conductivity) and $\pm 5\%$ (Seebeck coefficient). The Hall carrier concentration p_H (n_H) and mobility μ_H were calculated via $p_H = 1/eR_H$ ($n_H = -1/eR_H$) and $\mu_H = \sigma R_H$, where e is unit charge and R_H is the Hall coefficient measured by commercial Physical Properties Measurement System (PPMS; Quantum Design, USA) under magnetic fields from -5.2 T to 5.2 T. The thermal conductivity was calculated by the formula $\kappa = DC_p d_s$, where D is thermal diffusivity measured by laser flash instrument (NETZSCH, LFA457, Germany) by coating all samples with a thin layer of graphite to minimize emissivity errors (the actual measurement error is about 3%), C_p is specific heat derived by temperature-dependent heat data using the differential thermal analyzer (NETZSCH, DSC204F1, Germany), and d_s is the samples' density estimated by the Archimedes method. The relative densities of these samples are about 95%.

3. Results and discussion

3.1. Phase and microstructure

The cubic NbCoSn crystal structure is shown in Figure 1. The element Nb (4a site) and Co (4b site) frame the NaCl sublattice with octahedral coordination, leaving the all tetrahedral central sites (4c site) to the element Sn, but only half of the 4c site is occupied by Sn, forming this half-Heusler compound. Simply, by applying the Zintl chemistry concept [43], this crystal structure can be

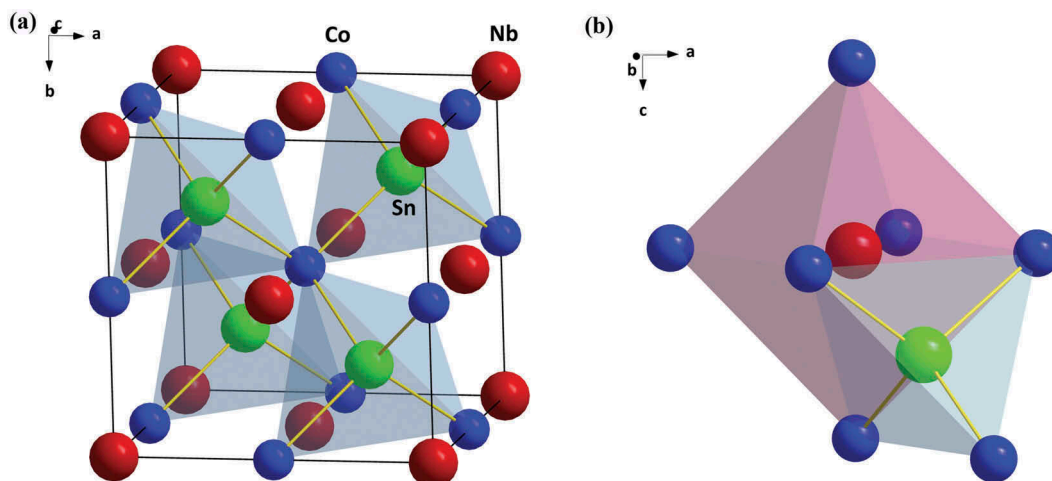


Figure 1. The crystal structure of NbCoSn (a) and the coordination environment of Nb and Sn (b).

described into an anionic framework $[\text{CoSn}]^{5-}$ formed by the tetrahedral coordination of Co and Sn, and an electropositive Nb^{5+} filled in the octahedral voids formed by these tetrahedral frameworks.

PXRD patterns of $\text{Nb}_{1-z}\text{Sc}_z\text{CoSn}$ ($z = 0, 0.01, 0.03, 0.04, 0.05, 0.06, 0.07, 0.10$) samples are shown in Figure 2(a). The diffraction peaks of all the samples can be indexed to MgAgAs cubic crystal structure despite some minor Nb_3Sn impurity phases, indicating all samples possess the HH phase. As it is visible from Figure 2(b), the unit cell parameter calculated via PowderCell [44] software increases with the increasing Sc content. Since the ionic radius of Sc^{3+} (0.87 \AA) is larger than that of Nb^{5+} (0.74 \AA) [45], the observed lattice expansion indicates Nb^{5+} is substituted by Sc^{3+} .

The phase purity and elemental distribution were further examined by SEM combined with EDX mapping. Figure 3 shows the secondary electron image and the EDX maps of a polished $\text{Nb}_{0.95}\text{Sc}_{0.05}\text{CoSn}$ sample, which indicates no obvious phase segregation and uniform elemental distribution on this scale. Table 1 summarizes the actual chemical compositions of all prepared samples analyzed by EDX, and it shows that the actual

chemical compositions are close to the nominal compositions.

3.2. Electrical transport properties

Figure 4 shows the electrical transport properties of $\text{Nb}_{1-z}\text{Sc}_z\text{CoSn}$ at different temperatures. For comparison, the literature data of $\text{Nb}_{0.8}\text{Zr}_{0.2}\text{CoSn}$ [42] are also plotted (black line). As displayed in Figure 4(a), the electrical conductivity (σ) of unsubstituted NbCoSn compound decreases with the rise of temperature, showing a metal-like conducting behaviour. While, after substituting Sc at Nb site, the σ gradually increases with increasing temperature, indicating a semiconductor behaviour. Besides, with the Sc concentration up to 0.05, the σ significantly decreases from $5.0 \times 10^4 \text{ S/m}$ (NbCoSn) to $0.07 \times 10^4 \text{ S/m}$ ($\text{Nb}_{0.95}\text{Sc}_{0.05}\text{CoSn}$) at room temperature and then goes up to $\sim 0.6 \times 10^4 \text{ S/m}$ with further increasing Sc concentration to 0.1 ($\text{Nb}_{0.9}\text{Sc}_{0.1}\text{CoSn}$). In addition, the band gap can be obtained from the slope of $\ln\sigma$ vs. $1000/T$ curve (shown in Figure 4(b)) using the Arrhenius equation

$$\rho = \rho_0 \exp(E_g/2k_B T) \tag{1}$$

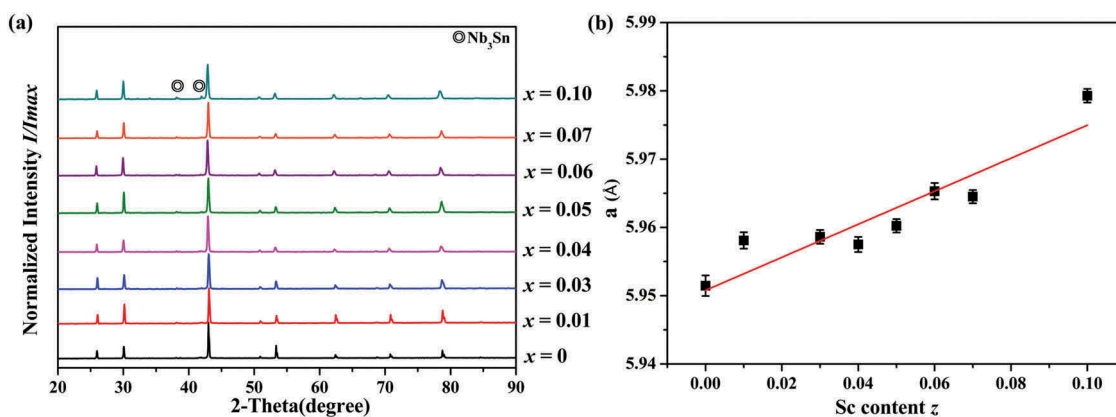


Figure 2. (a) PXRD patterns and (b) cell parameters of $\text{Nb}_{1-z}\text{Sc}_z\text{CoSn}$ samples.

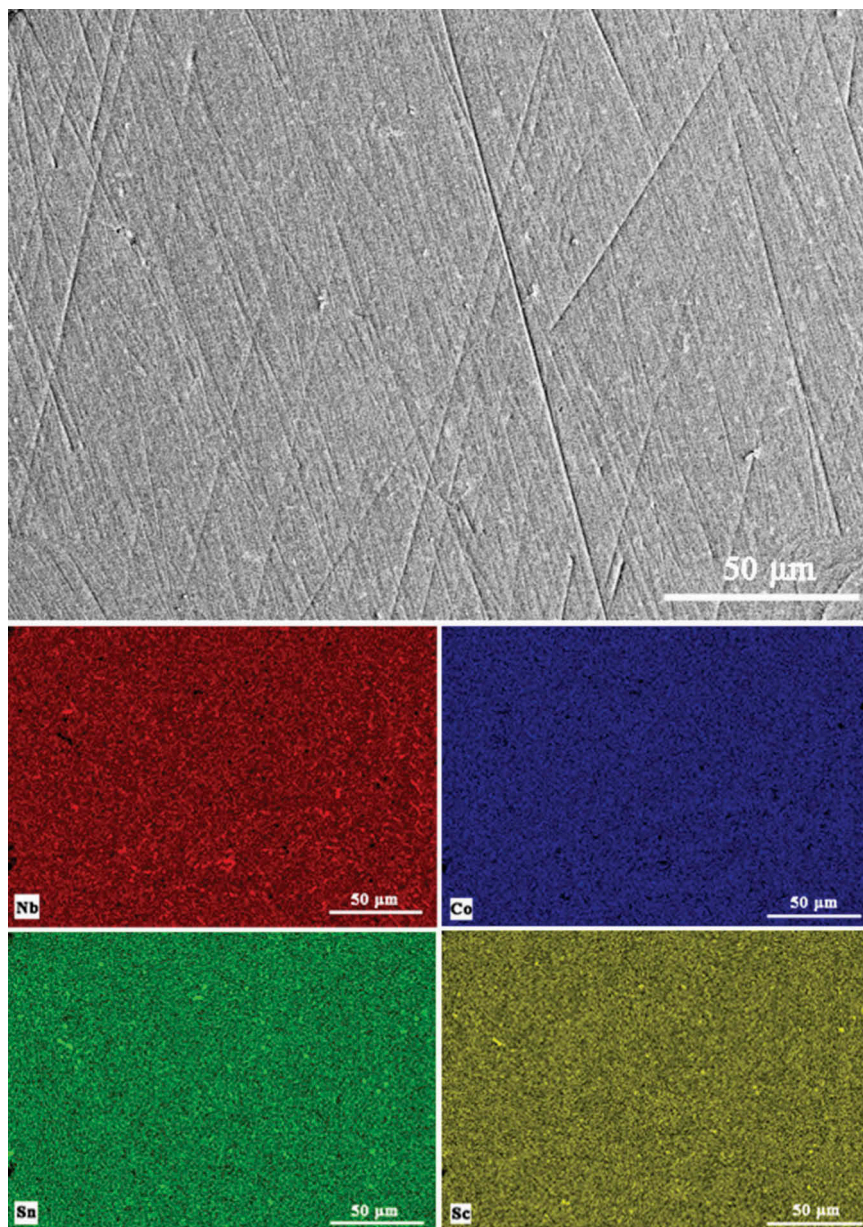


Figure 3. The secondary electron image and the elemental distribution maps of Nb_{0.95}Sc_{0.05}CoSn.

Table 1. Nominal, actual compositions by EDX and measured densities of Nb_{1-z}Sc_zCoSn.

Nominal	EDX results	d_s (g/cm ³)
Nb _{0.99} Sc _{0.01} CoSn	Nb _{0.98} Sc _{0.01} Co _{1.05} Sn _{0.96}	8.49
Nb _{0.97} Sc _{0.03} CoSn	Nb _{0.97} Sc _{0.03} Co _{1.06} Sn _{0.94}	8.46
Nb _{0.96} Sc _{0.04} CoSn	Nb _{0.98} Sc _{0.04} Co _{1.03} Sn _{0.95}	8.03
Nb _{0.95} Sc _{0.05} CoSn	Nb _{0.97} Sc _{0.045} Co _{1.03} Sn _{0.95}	8.39
Nb _{0.94} Sc _{0.06} CoSn	Nb _{0.94} Sc _{0.053} Co _{1.05} Sn _{0.95}	8.00
Nb _{0.93} Sc _{0.07} CoSn	Nb _{0.93} Sc _{0.067} Co _{1.05} Sn _{0.96}	8.37
Nb _{0.90} Sc _{0.10} CoSn	Nb _{0.95} Sc _{0.09} Co _{1.03} Sn _{0.94}	8.27

where ρ_0 is a constant. The calculated band gap values are 0.35 eV, 0.33 eV, 0.29 eV and 0.20 eV for p -type Nb_{0.95}Sc_{0.05}CoSn, Nb_{0.94}Sc_{0.06}CoSn, Nb_{0.93}Sc_{0.07}CoSn and Nb_{0.90}Sc_{0.10}CoSn respectively. For the Nb_{1-z}Sc_zCoSn compounds with $z > 0.04$, the slope of σ - T changes above 500 K and it can be explained by the impact of intrinsic conduction.

To further understand the conduction mechanism, the Hall coefficient at room temperature was

measured and the calculated charge carriers concentration and mobility are presented in Figure 5 (a,b). The electron concentration n_H for NbCoSn is $17 \times 10^{19} \text{ cm}^{-3}$, which is on the same order of magnitude as compared to the value reported by He et al. ($\sim 24 \times 10^{19} \text{ cm}^{-3}$) [37]. Moreover, the n_H decreases remarkably with the Sc content reaching 0.04. For $z = 0.05$, holes become the dominant carriers, and the hole concentration p_H increases gradually from $0.8 \times 10^{19} \text{ cm}^{-3}$ to $3.7 \times 10^{19} \text{ cm}^{-3}$ with the Sc content increasing from 0.05 to 0.10. Therefore, Sc is obviously an effective hole (p -type) dopant since it generates acceptor level near the top of the valence band and shifts the Fermi level toward the valence band, resulting in an increase of hole concentration. As for the carrier mobility μ_H , the trend is similar to that of carrier concentration. Therefore,

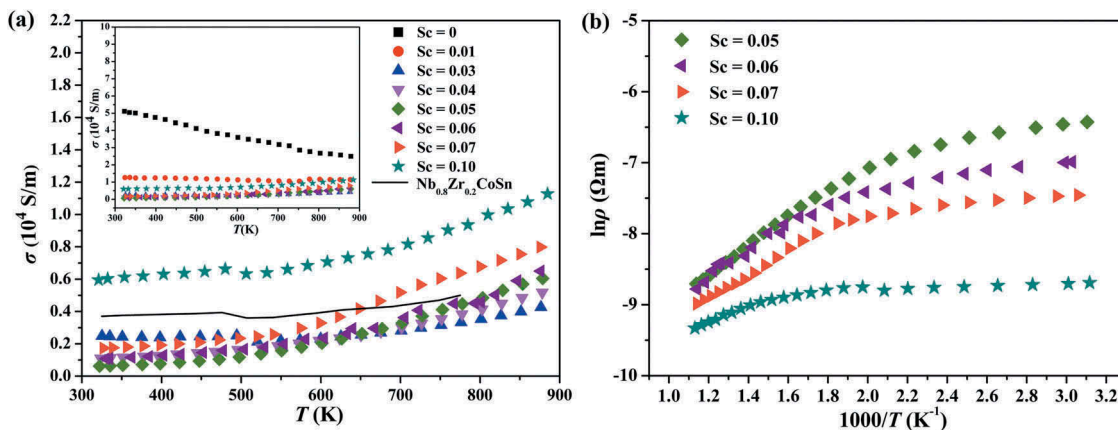


Figure 4. Temperature dependence of the electrical transport properties of $\text{Nb}_{1-z}\text{Sc}_z\text{CoSn}$ (a) electrical conductivity (b) $\ln \rho$ vs. $1000/T$ plot.

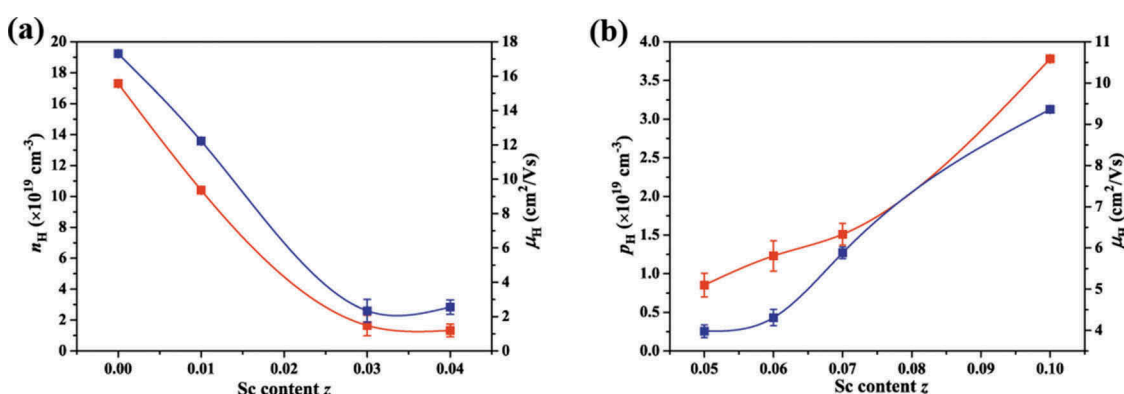


Figure 5. The carrier concentration and carrier mobility of $\text{Nb}_{1-z}\text{Sc}_z\text{CoSn}$ samples at room temperature (a) n -type, (b) p -type.

the σ decreases obviously and then increases slightly with increase of Sc content.

The temperature dependence of Seebeck coefficient (S) in $\text{Nb}_{1-z}\text{Sc}_z\text{CoSn}$ is shown in Figure 6(a). The value of S for unsubstituted NbCoSn is $-185 \mu\text{V/K}$ at room temperature, showing that NbCoSn is apparently an n -type semiconductor. With Sc content increasing, the S of $\text{Nb}_{1-z}\text{Sc}_z\text{CoSn}$ changes gradually from negative to positive with

increasing of Sc content, which matches very well with the Hall measurements. The peak value of S reaches $\sim 306 \mu\text{V/K}$ at 850 K for the $\text{Nb}_{0.95}\text{Sc}_{0.05}\text{CoSn}$ sample, and it is much higher than that ($150 \mu\text{V/K}$) of $\text{Nb}_{0.8}\text{Zr}_{0.2}\text{CoSn}$. The single parabolic band (SPB) model is usually used to analyze the transport properties of half-Heusler compounds [46]. Assuming electron conduction occurs within an SPB, the Seebeck coefficient of a non-degenerate

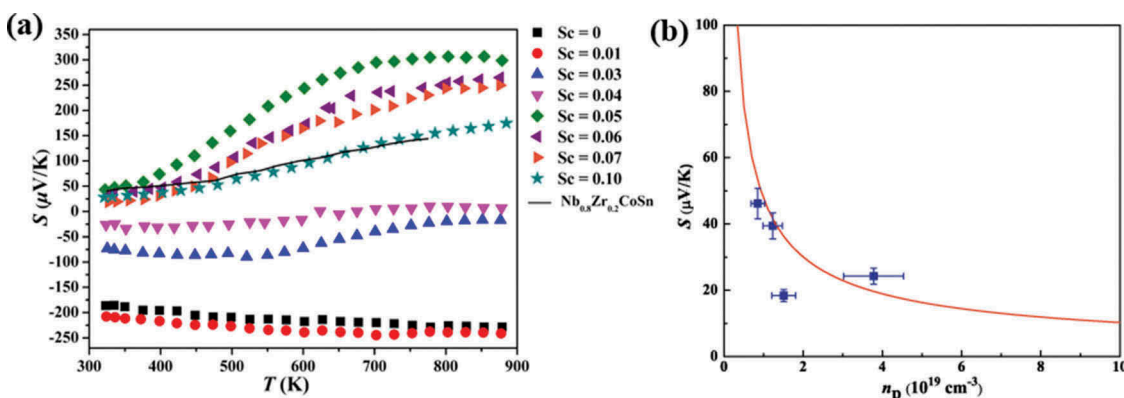


Figure 6. Temperature dependence of the Seebeck coefficient (a) and the Seebeck coefficient versus the carrier concentration (p -type) (b) of $\text{Nb}_{1-z}\text{Sc}_z\text{CoSn}$ samples.

semiconductor is related to the effective mass m^* , carrier concentration p_H and scattering parameter λ via

$$S = \frac{k_B}{e} \left\{ 2 + \lambda + \ln \left[\frac{2(2\pi m^* k_B T / h^2)^{3/2}}{p_H} \right] \right\} \quad (2)$$

where e is the elementary charge and h is the Planck constant [47]. For the NbCoSn compound, we assume that acoustic phonon scattering is the predominant scattering mechanism, thus $\lambda = 0$. According to the measured S and p_H , the $m^* = 0.11m_e$ is obtained. With the $m^* = 0.11m_e$ and the Equation (2), we can plot S at 300 K as a function of p_H , a plot well-known as a ‘Pisarenko relation’. As shown in Figure 6(b), the red line is the calculated Pisarenko plot, and the blue dots represent measured data of Nb_{1-z}Sc_zCoSn compounds. Most of the data lie on the calculated line, except for that of Nb_{0.93}Sc_{0.07}CoSn compound. The reason for such an exception is not clear yet. It is suspected that the second phase or/and the deviation of the composition may be responsible for such an exception.

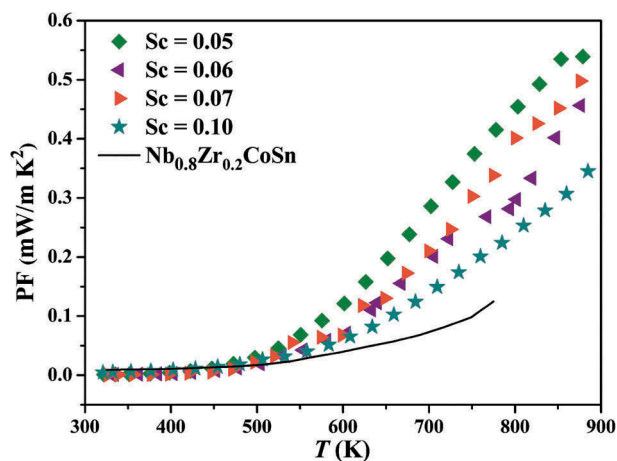


Figure 7. Temperature dependence of the power factor of Nb_{1-z}Sc_zCoSn.

Accordingly, the power factor (PF) was calculated via $PF = S^2\sigma$ and is shown in Figure 7. The highest PF of 0.54 mW/mK² is achieved for Nb_{0.95}Sc_{0.05}CoSn compound mainly due to its high S , and it is 3 times higher than that of p -type Nb_{0.8}Zr_{0.2}CoSn (0.125 mW/mK²) [42]. However, the PF of Nb_{0.95}Sc_{0.05}CoSn is still much lower than the state of the art p -type HH compounds, such as (Ti/Hf)Co(SbSn) [39] and NbFeSb [48]. Therefore, much more effort must be devoted to optimizing the carrier concentration of p -type NbCoSn compounds.

3.3. Thermal transport properties

The temperature dependence of total thermal conductivity (κ) and lattice thermal conductivity (κ_L) are displayed in Figure 8. The κ_c is calculated by using the Wiedemann-Franz law: $\kappa_c = L\sigma T$, where L is Lorenz number estimated by Fermi integral, and then κ_L is derived from the value subtracting the carrier component κ_c from the total thermal conductivity. Because of the low electrical conductivity, the calculated κ_c is much lower than κ_L . In other words, for Nb_{1-z}Sc_zCoSn compounds $\kappa_L \approx \kappa$. As shown in Figure 8(b), the κ_L of unsubstituted NbCoSn is ~ 10.8 W/mK at room temperature, and this value is similar as compared to the result reported by Ferluccio et al. [42]. After substituting Sc, the room temperature κ_L decreases dramatically to 4.2 W/mK for Nb_{0.9}Sc_{0.1}CoSn, where a reduction of 60% is achieved after Sc substitution. Such a significant reduction mainly ascribes to the point defect scattering due to the substantial atomic mass difference (mass fluctuation) and interatomic coupling force differences (strain field fluctuation) between Nb and Sc, thereby giving rise to the reduction of κ_L , especially at room temperature.

To explain the reduction of κ_L in terms of the phonon scattering mechanisms, the lattice thermal conductivity of Nb_{1-z}Sc_zCoSn can be evaluated via Debye-Callaway model [49]:

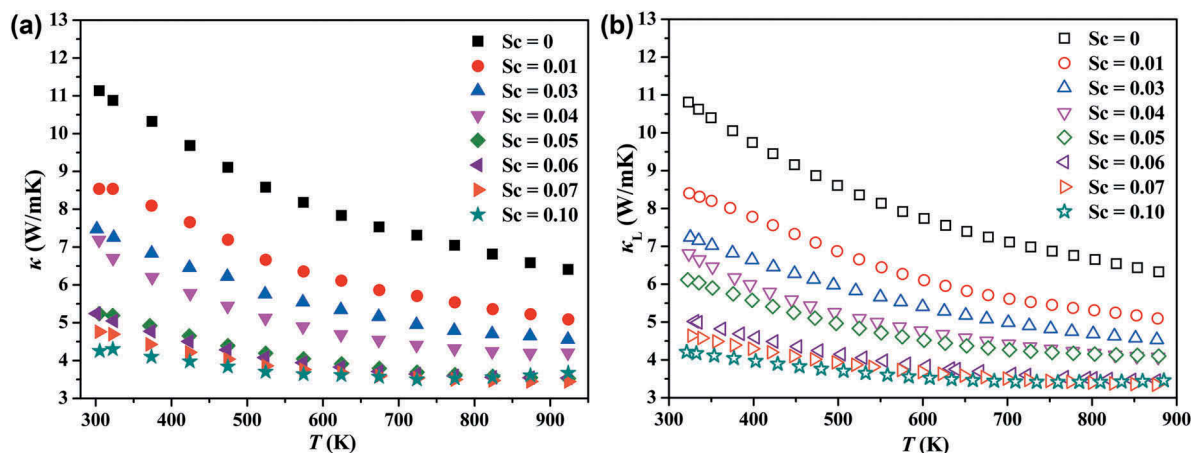


Figure 8. The temperature dependence of total thermal conductivity κ (a) and lattice thermal conductivity κ_L (b).

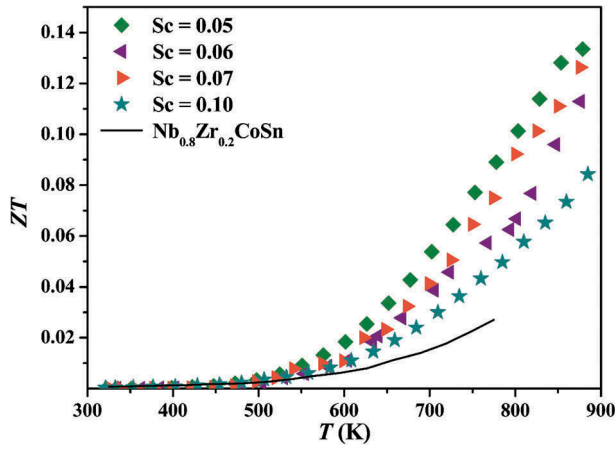


Figure 10. The figure of merit ZT for p -type NbCoSn and $\text{Nb}_{0.8}\text{Zr}_{0.2}\text{CoSn}$.

$$\kappa_L = \frac{k_B}{2\pi^2 v_s} \left(\frac{2\pi k_B T}{h} \right)^3 \int_0^{\theta_D/T} \tau_C \frac{x^4 e^x}{(e^x - 1)^2} dx \quad (3)$$

where x is the reduced frequency ($x = \hbar\omega/2\pi k_B T$), ω is the phonon angular frequency, v_s is the sound speed, h is the Planck constant, θ_D is the Debye temperature, and τ_C is the combined phonon relaxation time. The literature data [42] of $\theta_D = 361$ K and $v_s = 3141$ m/s for NbCoSn are used in $\text{Nb}_{1-z}\text{Sc}_z\text{CoSn}$ compounds as a good approximation. We assume all phonon scattering processes, including point-defect scattering, boundary scattering, Umklapp scattering, and phonon-free-electron scattering can occur in parallel and thus each adds to the process according to the Matthiessen's rule, then the τ_C can be formulated in Equation (4)

$$\tau_C^{-1} = \tau_{PD}^{-1} + \tau_B^{-1} + \tau_U^{-1} + \tau_{pe}^{-1} \quad (4)$$

where τ_{PD} , τ_B , τ_U , and τ_{pe} are phonon-point-defect scattering, phonon-boundary scattering, phonon-

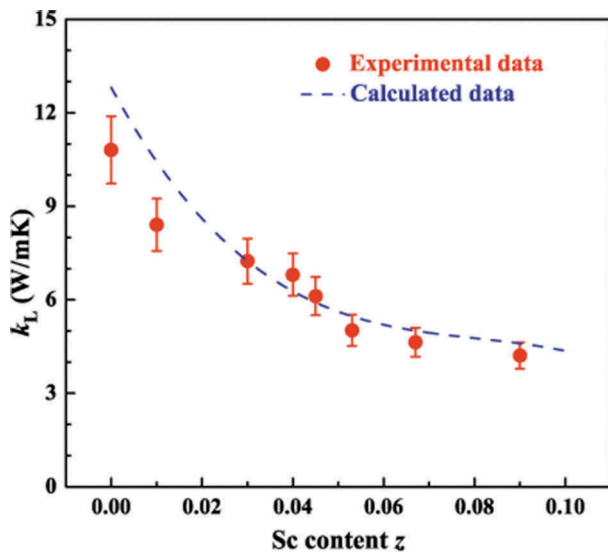


Figure 9. Comparison of experimental and calculated lattice thermal conductivities at 300 K for $\text{Nb}_{1-z}\text{Sc}_z\text{CoSn}$ compounds.

phonon Umklapp scattering and phonon-free-electron scattering relaxation times, respectively. The τ_{PD} can be obtained through:

$$\tau_{PD}^{-1} = \tau_S^{-1} + \tau_M^{-1} = \frac{V\omega^4}{4\pi v_s^3} (\Gamma_S + \Gamma_M) \quad (5)$$

where τ_S and τ_M are relaxation times of the phonon-point-defect scattering processes due to strain and mass field fluctuations, V is the volume per atom, Γ_S and Γ_M are the disorder scattering parameters due to strain and mass field fluctuations [50]. The experimental disorder scattering parameters Γ_{expt} ($\Gamma_{\text{expt}} = \Gamma_S + \Gamma_M$) can be obtained by

$$\Gamma_{\text{exp}} = \frac{\hbar v_s^2 u^2}{\pi^2 \theta_D V} \times \frac{1}{\kappa_L^P}, \text{ and } \frac{\kappa_{L0}}{\kappa_L^P} = \frac{\tan^{-1}(u)}{u} \quad (6)$$

where u is the disorder scattering parameter, κ_{L0} is the lattice thermal conductivity of the crystal with the disorder, and κ_{L0}^P is the lattice thermal conductivity of the crystal without disorder [51]. The disorder scattering parameters of $\text{Nb}_{1-z}\text{Sc}_z\text{CoSn}$ compounds calculated according to Equation (6) are listed in Table 2.

For the phonon-boundary scattering, τ_B is independent of temperature and phonon frequency, and it can be described as $\tau_B^{-1} = v_s/d$, where d is the grain size of the bulk sample. For the Umklapp scattering, τ_U is dependent on temperature and phonon frequency and can be described as [52]

$$\tau_U^{-1} \approx \frac{\hbar\gamma^2}{2\pi M v_s^2 \theta_D} \omega^2 T \exp(-\theta_D/3T) \quad (7)$$

where γ is the Grüneisen constant and M is the average atomic mass of the crystal. For the phonon-free-electron scattering process [53], in the case of high carrier concentration τ_{pe} can be described as

$$\tau_{pe}^{-1} = \frac{4\pi^2 E_{\text{def}}^2 m^* \omega}{\hbar^3 d_s v_l} \quad (8)$$

where E_{def} is the deformation potential, d_s is the sample's density, and v_l is the longitudinal sound velocity. With the reference values of physics parameters (Table S1 in Supplementary Information), the lattice thermal conductivity of $\text{Nb}_{1-z}\text{Sc}_z\text{CoSn}$ can be calculated by Equation (3) and the results are presented in Figure 9. In the

Table 2. The lattice thermal conductivity κ_L , disorder scattering parameter u , disorder scattering parameters Γ_{expt} .

Composition	κ_L	u	Γ_{expt}
NbCoSn	10.8		
$\text{Nb}_{0.99}\text{Sc}_{0.01}\text{CoSn}$	8.4	1.03	0.0025(4)
$\text{Nb}_{0.97}\text{Sc}_{0.03}\text{CoSn}$	7.2	1.44	0.0049(8)
$\text{Nb}_{0.96}\text{Sc}_{0.04}\text{CoSn}$	6.8	1.61	0.0062(7)
$\text{Nb}_{0.95}\text{Sc}_{0.05}\text{CoSn}$	6.1	1.93	0.0089(8)
$\text{Nb}_{0.94}\text{Sc}_{0.06}\text{CoSn}$	5.0	2.59	0.016(1)
$\text{Nb}_{0.93}\text{Sc}_{0.07}\text{CoSn}$	4.6	2.88	0.019(9)
$\text{Nb}_{0.90}\text{Sc}_{0.10}\text{CoSn}$	4.2	3.27	0.025(6)

calculation, we assume that Sc substitution does not significantly affect the basic physics parameters, such as θ_D , γ , E_{def} and ν_s , so the major variable parameter is Γ_{expt} . In such a case, Sc substitution mainly alters the τ_{PD} . Generally, the calculated κ_L matches with the experimental values, implying that calculations based on Callaway-Debye model can give a rough prediction to the κ_L of NbCoSn system. In short, at room temperature the reduction of κ_L of Nb_{1-x}Sc_xCoSn compounds is mainly due to that the Sc substitution induces strong point defect phonon scattering.

3.4. Figure of merit

Figure 10 shows the dimensionless figure of merit ZT of p -type samples. Due to the dramatic enhancement of power factor compared with p -type Nb_{0.8}Zr_{0.2}CoSn, and the significant suppression of thermal conductivity, the highest ZT of p -type Nb_{0.95}Sc_{0.05}CoSn achieves 0.13 at 879 K. It is much higher than that of Nb_{0.8}Zr_{0.2}CoSn [42], indicating Sc is an efficient p -type dopant for NbCoSn as compared to Zr.

4. Conclusions

In this work, homogenous Nb_{1-x}Sc_xCoSn compounds were prepared by an arc-melting process followed by an annealing treatment. The p -type NbCoSn compounds were obtained by substituting iso-electronic Sc at the Nb site and the effects on the electrical and thermal properties were investigated. Generally, the substitution of Sc at Nb site can change the n -type NbCoSn to a p -type semiconductor by adjusting the Fermi level, indicating Sc is an appropriate p -type dopant. Also, the thermal conductivity is reduced. As a result, the highest ZT is 0.13 at 879 K in p -type Nb_{0.95}Sc_{0.05}CoSn sample, which is roughly 5 times higher than that of p -type Nb_{0.8}Zr_{0.2}CoSn.

Acknowledgments

We would like to acknowledge the financial support from Deutsche Forschungsgemeinschaft (Project No. BA 4171/4-1), and also acknowledge support by the German Research Foundation and the Open Access Publishing Fund of Technische Universität Darmstadt.

Disclosure statement

No potential conflict of interest was reported by the authors.

ORCID

Wenjie Xie  <http://orcid.org/0000-0003-1826-7574>

References

- [1] Populoh S, Brunko OC, Gałazka K, et al. Half-Heusler (TiZrHf)NiSn unileg module with high powder density. *Materials*. 2013;6(4):1326–1332.
- [2] Bell LE. Cooling, heating, generating power, and recovering waste heat with thermoelectric systems. *Science*. 2008;321:1457–1467.
- [3] Vining CB. An inconvenient truth about thermoelectrics. *Nat Mater*. 2009;8:83–85.
- [4] Sootsman JR, Chung DY, Kanatzidis MG. New and old concepts in thermoelectric materials. *Angew Chem Int Ed*. 2009;48:8616–8639.
- [5] He J, Tritt TM. Advances in thermoelectric materials research: looking back and moving forward. *Science*. 2017;357:1369–1377.
- [6] Chung DY, Iordanidis L, Choi KS, et al. Complex chalcogenides as thermoelectric materials: A solid state chemistry approach. *Bull Korean Chem Soc*. 1998;19:1281–1448.
- [7] Petsagkourakis I, Tybrandt K, Crispin X, et al. Thermoelectric materials and applications for energy harvesting power generation. *Sci Technol Adv Mater*. 2018;19:836–862.
- [8] Zhu T, Liu Y, Fu C, et al. Compromise and synergy in high-efficiency thermoelectric materials. *Adv Mater*. 2017;29:1605884.
- [9] Yan R, Lin J, You L, et al. Increasing the thermoelectric power factor via Ag substitution at Zn site in Ba(Zn_{1-x}Ag_x)₂Sb₂. *J Alloy Compd*. 2018;745:228–233.
- [10] Muthusamy O, Nishino S, Ghodke S, et al. Low thermal conductivity of bulk amorphous Si_{1-x}Ge_x containing nano-sized crystalline particles synthesized by ball-milling process. *J Electron Mater*. 2018;47(6):3260–3266.
- [11] Heremans JP, Jovovic V, Toberer ES, et al. Enhancement of thermoelectric efficiency in PbTe by distortion of the electronic density of states. *Science*. 2008;321:554–557.
- [12] Maignan A, Guilmeau E, Gascoin F, et al. Revisiting some chalcogenides for thermoelectricity. *Sci Technol Adv Mater*. 2012;13(5):053003.
- [13] Vikrant T, Manjusha B, Priyadarshini B, et al. Microstructure and doping effect on the enhancement of the thermoelectric properties of Ni doped Dy filled CoSb₃ skutterudites. *Sustain Energ Fuels*. 2018;2:2687–2697.
- [14] Kim SW, Kimura Y, Mishima Y. Enhancement of high temperature thermoelectric properties of intermetallic compounds based on a Skutterudite IrSb₃ and a half-Heusler TiNiSb. *Sci Technol Adv Mater*. 2004;5:485–489.
- [15] Ikeda MS, Euchner H, Yan X, et al. Kondo-like phonon scattering in thermoelectric clathrates. *Nat Commun*. 2019;10:887.
- [16] Tang J, Li Z, Ju J, et al. Soft X-ray photoelectron spectroscopy study of type-I clathrates. *Sci Technol Adv Mater*. 2008;9(4):044207.
- [17] Yan R, Lv W, Wang K, et al. Enhanced thermoelectric properties of BaZn₂Sb₂ via a synergistic optimization strategy using co-doped Na and Sr. *J Mater Chem A*. 2016;4:12119.
- [18] Poon SJ. Recent advances in thermoelectric performance of half-Heusler compounds. *Metals*. 2018;8:989.
- [19] Zhu H, Mao J, Li Y, et al. Discovery of TaFeSb-based half-Heuslers with high thermoelectric performance. *Nat Commun*. 2019;10:270.

- [20] Mao J, Liu Z, Zhou J, et al. Advances in thermoelectrics. *Adv Phys.* 2018;67:69–147.
- [21] Xie W, He J, Zhu S, et al. Simultaneously optimizing the independent thermoelectric properties in (Ti, Zr, Hf)(Co, Ni) Sb alloy by in situ forming InSb nanoinclusions. *Acta Mater.* 2010;58:4705–4713.
- [22] Xie W, Yan Y, Zhu S, et al. Significant ZT enhancement in p -type Ti(Co,Fe)Sb–InSb nanocomposites via a synergistic high-mobility electron injection, energy-filtering and boundary-scattering approach. *Acta Mater.* 2013;61:2087–2094.
- [23] Hori T, Shiomi J. Tuning phonon transport spectrum for better thermoelectric materials. *Sci Technol Adv Mater.* 2018;20:10–25.
- [24] Wan C, Wang Y, Wang N, et al. Development of novel thermoelectric materials by reduction of lattice thermal conductivity. *Sci Technol Adv Mater.* 2010;11:044306.
- [25] Hinterleitner B, Knapp I, Poneder M, et al. Thermoelectric performance of a metastable thin-film Heusler alloy. *Nature.* 2019;576:85–90.
- [26] Tsujii N, Nishide A, Hayakawa J, et al. Observation of enhanced thermopower due to spin fluctuation in weak itinerant ferromagnet. *Sci Adv.* 2019;5:eaat5935.
- [27] Xie W, Weidenkaff A, Tang X, et al. Recent advances in nanostructured thermoelectric half-Heusler compounds. *Nanomaterials.* 2012;2:379–412.
- [28] Populoh S, Aguirre MH, Brunko O, et al. High figure of Merit in (Ti,Zr,Hf)NiSn half Heusler alloys. *Scripta Mat.* 2012;66:1073–1076.
- [29] Galazka K, Populoh S, Xie W, et al. Improved thermoelectric performance of $(Zr_{0.3}Hf_{0.7})NiSn$ half-Heusler compounds by Ta substitution. *J Appl Phys.* 2014;115:183704.
- [30] Zou T, Jia T, Xie W, et al. Band structure modification of the thermoelectric Heusler-phase $TiFe_2Sn$ via Mn substitution. *Phys Chem Chem Phys.* 2017;19:18273–18278.
- [31] Chen S, Ren Z. Recent progress of half-Heusler for moderate temperature thermoelectric applications. *Mater Today.* 2013;16(10):387–395.
- [32] Jeitschko W. Transition metal stannides with $MgAgAs$ and $MnCu_2Al$ type structure. *Metall Trans.* 1970;1:3159–3162.
- [33] Kandpal HC, Felser C, Seshadri R. Covalent bonding and the nature of band gaps in some half-Heusler compounds. *J Phys D Appl Phys.* 2006;39:776–785.
- [34] Sofo JO, Mahan GD. Optimum band gap of a thermoelectric materials. *Phys Rev B.* 1994;49(7):4565–4570.
- [35] Xi L, Yang J, Wu L, et al. Band engineering and rational design of high-performance thermoelectric materials by first-principles. *J Materiomics.* 2016;2:114–130.
- [36] Ono Y, Inayama S, Adachi H, et al. Thermoelectrics properties of doped half-Heuslers $NbCoSn_{1-x}Sb_x$ and $Nb_{0.99}Ti_{0.01}CoSn_{1-x}Sb_x$. *Jpn J Appl Phys.* 2006;45(11):8740–8743.
- [37] He R, Huang L, Wang Y, et al. Enhanced thermoelectric properties of n -type $NbCoSn$ half-Heusler by improving phase purity. *APL Mater.* 2016;4:104804.
- [38] Yu C, Zhu TJ, Shi RZ, et al. High-performance half-Heusler thermoelectric materials $Hf_{1-x}Zr_xNiSn_{1-y}Sb_y$ prepared by levitation melting and spark plasma sintering. *Acta Mater.* 2009;57:2757–2764.
- [39] Yan X, Liu W, Wang H, et al. Stronger phonon scattering by larger differences in atomic mass and size in p -type half-Heuslers $Hf_{1-x}Ti_xCoSb_{0.8}Sn_{0.2}$. *Energy Environ Sci.* 2012;5:7543–7548.
- [40] Poon SJ, Wu D, Zhu S, et al. Half-Heusler phases and nanocomposites as emerging high- ZT thermoelectric materials. *J Mater Res.* 2011;26:2795–2802.
- [41] Xing Y, Liu R, Liao J, et al. High-efficiency half-Heusler thermoelectric modules enabled by self-propagating synthesis and topologic structure optimization. *Energy Environ Sci.* 2019;12:3390–3399.
- [42] Ferluccio DA, Smith RI, Buckman J, et al. Impact of Nb vacancies and p -type doping of the $NbCoSn$ - $NbCoSb$ half-Heusler thermoelectrics. *Phys Chem Chem Phys.* 2018;20:3979–3987.
- [43] Zeier WG, Schmitt J, Hautier G, et al. Engineering half-Heusler thermoelectric materials using Zintl chemistry. *Nat Rev Mater.* 2016;1:16032.
- [44] Kraus W, Nolze G. Powder Cell - a program for the representation and manipulation of crystal structures and calculation of the resulting X-ray powder patterns. *J Appl Cryst.* 1996;29:301–303.
- [45] Shannon RD. Revised effective ionic radii and systematic studies of interatomic distances in Halides and chalcogenides. *Acta Cryst.* 1976;A32:751–767.
- [46] Qiu Q, Liu Y, Xia K, et al. Grain boundary scattering of charge transport in n -type $(Hf,Zr)CoSb$ half-Heusler thermoelectric materials. *Adv Energy Mater.* 2019;9:1803447.
- [47] Ioffe AF. Semiconductor thermoelements, and thermoelectric cooling. London: Infosearch Ltd; 1957.
- [48] Fu C, Bai S, Liu Y, et al. Realizing high figure of merit in heavy-band p -type half-Heusler thermoelectric materials. *Nat Commun.* 2015;6:8144.
- [49] Callaway J. Model for lattice thermal conductivity at low temperatures. *Phys Rev.* 1959;113:1046–1051.
- [50] Yang J, Meisner GP, Chen L. Strain field fluctuation effects on lattice thermal conductivity of $ZrNiSn$ -based thermoelectric compounds. *Appl Phys Lett.* 2004;85:1140–1142.
- [51] Fu C, Xie H, Zhu TJ, et al. Enhanced phonon scattering by mass and strain field fluctuations in Nb substituted $FeVSb$ half-Heusler thermoelectric materials. *J Appl Phys.* 2012;112:124915.
- [52] Toberer ES, Zevalkink A, Snyder GJ. Phonon engineering through crystal chemistry. *J Mater Chem.* 2011;21:15843–15852.
- [53] Parrott JE. Heat conduction mechanisms in semiconducting materials. *Rev Int Hautes Temp Refract.* 1979;16:393.